Electronic Supplementary Material (ESI) for Soft Matter.


# SUPPLEMENTARY INFORMATION

# A simulation study of aggregation mediated by production of cohesive molecules

Gavin Melaugh, Davide Marenduzzo, Alexander Morozov, and Rosalind J. Allen

*School of Physics and Astronomy,*

*University of Edinburgh*

(Dated: July 18, 2019)

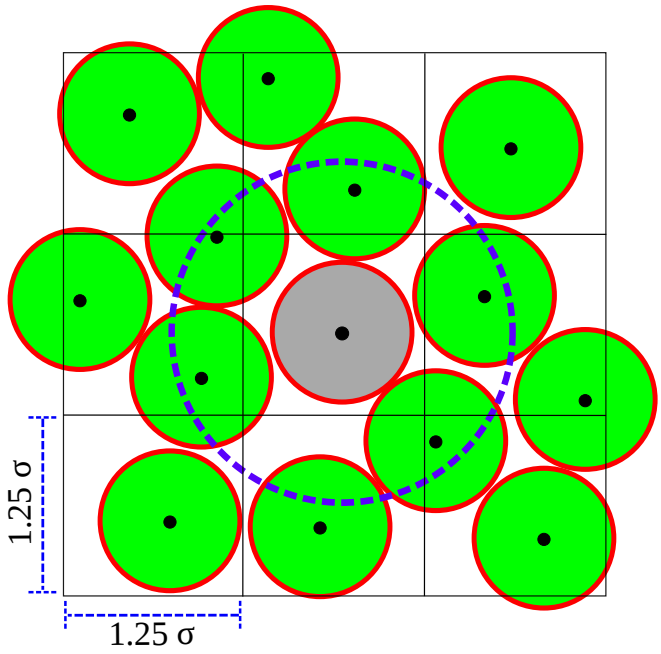


FIG. 1. Schematic depiction of the 9 element density sub-grid used to compute the local density of particle $i$ (grey). All surrounding particles with coordinates (black dots) that lie within the sub-grid contribute to the local density, and hence to the $\epsilon$ value of particle $i$. The Lennard-Jones potential between the central particle $i$ and neighbours $j$ that lie beyond the cut-off region (blue circle), determined by the cut-off radius $r_c = 1.2\sigma$, is set to zero.

## I. PARTICLE-BASED SIMULATIONS

### A. Computing the density and the corresponding $\epsilon$

Our Brownian Dynamics simulations were performed using in-house software written in Java. At each time-step of the density-dependent simulations, the interaction between any pair of particles, $i$ and $j$, depends on the local densities, $\rho_i$ and $\rho_j$, experienced by each particle. Local densities were computed on a $115\sigma \times 115\sigma$ grid comprised of $92 \times 92$ grid elements each with a length of $1.25\sigma$. The local density, $\rho_i$, experienced by particle $i$, was computed using a $3 \times 3$ element sub-grid centered around the element containing particle $i$ (Fig. 1). The value of $\rho_i$ was computed as the ratio of the sub-grid area, $9 \times (1.25\sigma \times 1.25\sigma)$, to number of particles in the sub-grid, and the value of $\epsilon_i$ assigned to that particle was obtained via $\epsilon_i = \rho_i \epsilon'$. The geometric average, $\epsilon_{i,j} = \sqrt{\epsilon_i \epsilon_j}$, was then used to compute the

Lennard-Jones potential (Eq. (15) of the main manuscript) for particle pairs separated by a distance less than the cut-off, $r_c = 1.2\sigma$ (blue circle). The computation of neighbour interactions was made more efficient via implementation of a linked neighbour list [1].

### B. Non-dimensionalisation of the over-damped Langevin equation

The position, $\mathbf{x}_i$ of an individual particle, $i$, at time $t$ was obtained in our simulations by solving the over-damped Langevin equation

$$\frac{\mathrm{d}\mathbf{x}_i}{\mathrm{d}t} = \beta D\mathbf{F}_i + \sqrt{2D}\eta_i(t), \tag{1}$$

where $D$ is the diffusion coefficient, $\beta = 1/k_BT$, $\mathbf{F}_i = -\nabla\sum_{j\neq i}^{N} U_{ij}$ is the force on particle $i$ resulting from interactions with its $N-1$ neighbours, and $\eta_i(t)$ is a unit variance white noise variable with $\langle\eta_i(t)\rangle = 0$ and $\langle\eta_{i;\alpha}(t)\eta_{i;\beta}(t')\rangle = \delta_{\alpha,\beta}\delta(t-t')$ with $\alpha, \beta = x, y$.

To integrate this equation numerically in our particle-based simulations, we used the discretised form of Eq. 1 for each component of the position vector $\mathbf{x_i}$

$$\mathrm{d}x_i = \beta D F_i \Delta t + \sqrt{2D}\tilde{\eta}\sqrt{\Delta t}, \tag{2}$$

where the dimensionless noise, $\tilde{\eta}(t)$, is a Gaussian random variable with mean 0 and variance of 1 [2]. For computational efficiency, the values of the random variable were generated from a uniform distribution with range $[-\sqrt{3}, \sqrt{3}]$ in order to ensure a mean value of 0 and a variance of 1 [2].

We non-dimensionalised this equation by rescaling the variables $x$, $t$, and $F$ via the following transformations

$$x \to \alpha\tilde{x} \tag{3a}$$

$$t \to \tau\tilde{t} \tag{3b}$$

$$F \to \phi\tilde{F}. \tag{3c}$$

Using $\sigma$, $\frac{\sigma^2}{D}$, and $k_BT$ as the basic units of length, time, and energy respectively, gives

$$\alpha = \sigma \tag{4a}$$

$$\tau = \frac{\sigma^2}{D} \tag{4b}$$

$$\phi = \frac{k_BT}{\sigma} \tag{4c}$$

so that the rescaled variables are given by

$$x \to \sigma\tilde{x} \tag{5a}$$

$$t \to \frac{\sigma^2}{D}\tilde{t} \tag{5b}$$

$$F \to \frac{k_B T}{\sigma}\tilde{F}. \tag{5c}$$

Substitution of Eqs. (5) into Eq. (2), gives

$$\mathrm{d}\tilde{x}_i = \frac{1}{\sigma}\frac{D}{k_B T}\frac{k_B T}{\sigma}\frac{\sigma^2}{D}\tilde{F}_i\Delta\tilde{t} + \frac{1}{\sigma}\frac{\sqrt{\sigma^2}}{\sqrt{D}}\sqrt{2D}\tilde{\eta}_i(t)\sqrt{\Delta\tilde{t}}, \tag{6}$$

which is equivalent to the non-dimensionalised form

$$\mathrm{d}\tilde{x}_i = \tilde{F}_i\Delta\tilde{t} + \sqrt{2}\tilde{\eta}_i(t)\sqrt{\Delta\tilde{t}}. \tag{7}$$

The use of $k_B T$ as the basic unit of energy rescales the interaction strength, $\epsilon$, in the Lennard-Jones potential to the dimensionless quantity $\tilde{\epsilon}$ via the transformation $\epsilon \to k_B T\tilde{\epsilon}$. The non-dimensionalised form of the Lennard Jones potential then has the form

$$\tilde{U}(\tilde{r}) = 4\tilde{\epsilon}\left[(1/\tilde{r})^{12} - (1/\tilde{r})^6 - \tilde{U}_{\mathrm{c}}\right], \tag{8}$$

where, $\tilde{r}$ is the distance between the two particles, and $\tilde{U}_c$ is the cut and shifted term that ensures that the interaction energy at the cut-off distance, $r_c = 1.2$, is zero. Considering $\epsilon$ as a function of the density, $\epsilon = \rho \times \epsilon'$, in our 2-dimensional density-dependent simulations, gives rise to the following rescaling transformations

$$\epsilon' \to k_B T\sigma^2\tilde{\epsilon} \tag{9a}$$

$$\epsilon \to \frac{k_B T\sigma^2}{\sigma^2}\tilde{\epsilon}. \tag{9b}$$

### C. Equilibration

The Brownian dynamics simulation method outlined above is stochastic due to the noise variable, $\eta$, and therefore many simulation runs should be performed in order to generate acceptable statistical data. We therefore performed 10 simulations for every parameter set $\theta$, $\epsilon'$ ($\epsilon$), in our density-dependent (-independent simulations). Stochasticity in each individual simulation was implemented by the use of a random-number generator, each of which was initialised with a different seed.

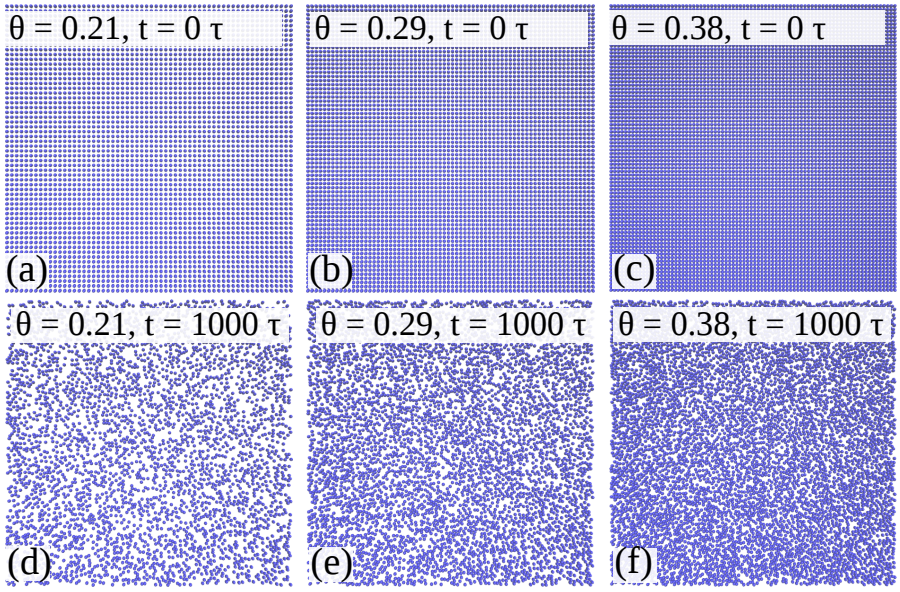


FIG. 2. Relaxation of the systems from initial lattice configurations. (a)-(c) Initial lattice configurations for systems with area fraction $\theta = 0.21$, $\theta = 0.29$, and $\theta = 0.38$. (d)-(f) Corresponding equilibrated configurations after "equilibration" runs of $1000\tau$ with WCA potential. This procedure was repeated 10 times for each area fraction. The resulting configurations were used to initialise 10 replicate simulations for each system under study.

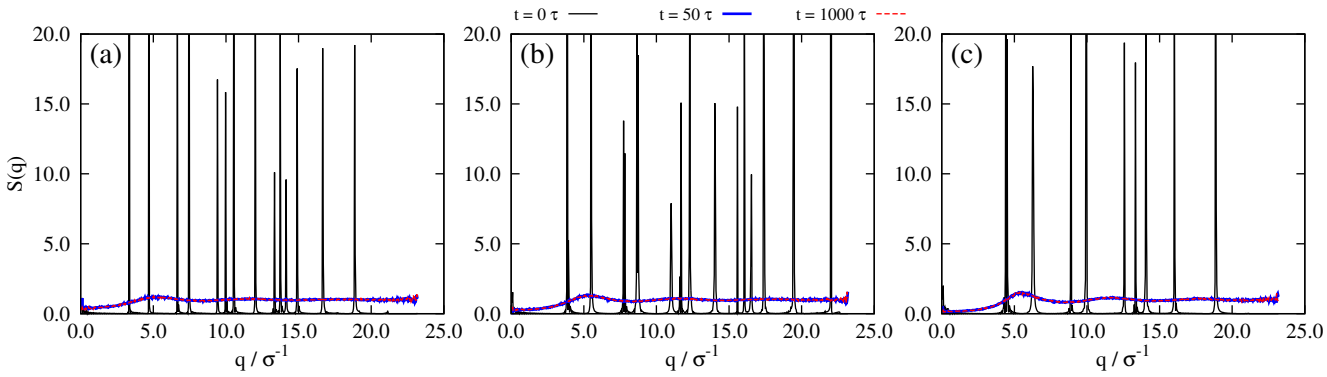


FIG. 3. Static structure factors, $S(q)$, corresponding to the relaxation of the systems from their initial lattice configurations (Fig. 2). (a) $\theta = 0.21$, (b) $\theta = 0.29$, (c) $\theta = 0.38$. An equilibration period of $1000\tau$ is clearly sufficient for the initial structure imposed by the lattice configuration to relax. The different colours correspond to various time points of the simulation.

To initiate our simulations of systems of particles interacting with density-dependent and

-independent potentials, we first generated 10 equilibrated starting configurations for each of three area fractions. To do this, $N$ particles corresponding to area fractions $\theta = 0.21(N = 3600)$, $\theta = 0.29(N = 4900)$, and $\theta = 0.38(N = 6400)$, were arranged on a 2D square lattice within a box of dimensions $115\sigma \times 115\sigma$ (see Figs. 2(a)-(c)). These systems were then relaxed for $1000\tau$ using the Brownian Dynamics simulation method (time-step of $1 \times 10^{-4}\tau$) outlined in Section I B above and in the main manuscript. During these equilibration runs, particles interacted via the soft repulsive Weeks-Chandler-Andersen potential [3]

$$U(r) = \begin{cases} 4\epsilon\left[(\sigma/r)^{12} - (\sigma/r)^{6}\right] + \epsilon & \text{if } r < 2^{\frac{1}{6}}\sigma \\ 0 & \text{if } r \geq 2^{\frac{1}{6}}\sigma, \end{cases} \tag{10}$$

which when using $\frac{\epsilon}{k_B T} = \tilde{\epsilon} = 1$ gives the non-dimensionalised form

$$\tilde{U}(\tilde{r}) = \begin{cases} 4\left[(1/\tilde{r})^{12} - (1/\tilde{r})^{6}\right] + 1 & \text{if } \tilde{r} < 2^{\frac{1}{6}} \\ 0 & \text{if } \tilde{r} \geq 2^{\frac{1}{6}}. \end{cases} \tag{11}$$

Figures 2(d)-(f) show representative final configurations resulting from this relaxation procedure. It is clear from Figs. 3, which show the static structure factor, $S(q)$ (see Sec. I D), at three different time points during the simulations depicted in Figs. 2(a)-(c), that $1000\tau$ is sufficient for the systems to relax from their initial lattice configurations. This relaxation procedure was performed 10 times for each area fraction, and the "equilibrated" final configurations were then used as starting configurations for simulations with the density-dependent and -independent Lennard-Jones interactions turned on. For example, to generate data for the density-dependent system $\theta = 0.29$, $\epsilon' = 40$, the 10 "equilibrated" configurations generated from the relaxation of the $\theta = 0.29$ system, were used to initialised 10 "production-run" simulations, each with a different set of random numbers, for this parameter set.

### D. Structure factor computation

Static structure factors were computed via

$$S(q) = N^{-1}\langle\rho(q)\rho(-q)\rangle, \tag{12}$$

where $q$ is the magnitude of the wave vector $\mathbf{q} = (2\pi/L)(k_x, k_y)$, with $L = 115\sigma$ being the box length, and $k_x$ and $k_y$ integers. The reciprocal space density, $\rho(q)$, is given by the spatial

Fourier transform of the number density via

$$\rho(q) = \sum_{i=1}^{N} \exp(i\mathbf{q} \cdot \mathbf{r}_i). \tag{13}$$

The structure factors at time $t = 0$ in Figs 3 were computed for the initial lattice configuration as described in Section I C above. The structure factors at each time $t > 0$ were computed as the average of configurations sampled every $10\tau$ during time windows of length $50\tau$ in any one simulation. For example, the structure factors at $t = 50\tau$ were computed as the average over the 5 simulation configurations sampled every $10\tau$ between $t = 10\tau \rightarrow 50\tau$. The structure factors at $t = 1000\tau$ were computed as the average over the 5 simulation configurations sampled every $10\tau$ between $t = 960\tau \rightarrow 1000\tau$.

For density-dependent simulations (see Sec. I F), in which a smaller time-step of $2.5 \times 10^{-5}\tau$ is used, the structure factors (Figs 6) at each time $t > 0$ were computed as the average of configurations sampled every $2.5\tau$ during time windows of length $60\tau$ in any one simulation, e.g., the $S(q)$ at $t = 62.5\tau$ was computed as the average over the 25 simulation configurations sampled every $2.5\tau$ between $t = 2.5\tau \rightarrow 62.5\tau$; at $t = 625\tau$, $S(q)$ was computed as the average over the 25 simulation configurations sampled every $2.5\tau$ between $t = 565\tau \rightarrow 625\tau$; and so on.

### E. Simulation run lengths

To explore the early phase separation behaviour in our density-dependent and density-independent simulations, we chose as our run-time, $t_{run}$, the approximate time required for the fraction of particles in clusters, $\Gamma$, to reach a steady state. Figure 4 shows the time evolution of $\Gamma$ during density-dependent simulations for the systems in the "gel-like" ($\epsilon' = 70$), and phase separating regimes ($\epsilon' = 45$, $\epsilon' = 40$, and $\epsilon' = 35$) at $\theta = 0.21$, $\theta = 0.29$, and $\theta = 38$.

The steady state value of $\Gamma$ is indicative of the extent of the phase separation. For example, small $\Gamma \rightarrow$ "gas rich" (data not shown); high $\Gamma \rightarrow$ "gel-like"; and intermediate $\Gamma$ is indicative of a phase separated state consisting of aggregates immersed in a sea of particles. In this intermediate steady state regime, where $\Gamma \rightarrow 0.65$ (the main focus of this study), one can see that $\Gamma$ has reached a steady state for $\theta = 0.21$ by $\sim 2500\tau$, whereas in the systems of higher area fractions, $\theta = 0.29$ and $\theta = 0.38$, equilibration of $\Gamma$ is attained at the earlier time

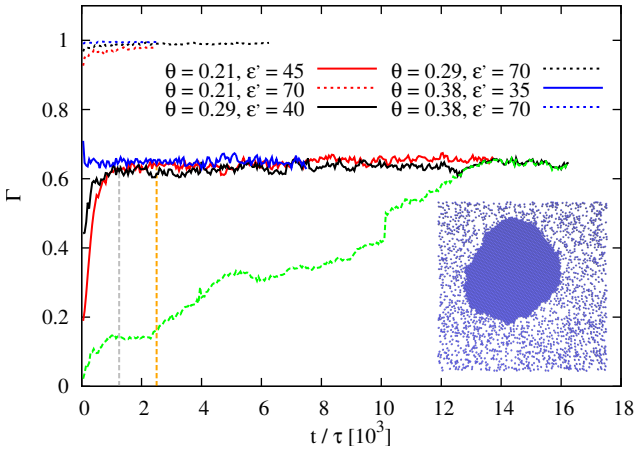


FIG. 4. The fraction of particles in aggregates, Γ, as a function of time. Γ approaches 1 for systems in the "gel-like" regime, $\epsilon' = 70$. In the phase separating regimes, $\epsilon' = 45, 40, 35$, for systems of area fraction $\theta = 0.21, 0.29, 0.38$ respectively, Γ has a steady-state value of $\sim 0.65$. The time for the systems to reach this steady-state is $\sim 2500\tau$ for the $\theta = 0.21$ system (dashed orange curve), and $\sim 1250\tau$ for the $\theta = 0.29$ and $\theta = 0.38$ systems (dashed grey curve). These times were considered long enough for simulation runs investigating the early aggregation behaviour in these systems. The dashed green curve shows the ratio of the maximum aggregate size to the number of particles, $N_a^{max}/N$, for the $\theta = 0.29, \epsilon' = 40$ system. This value equals Γ when coarsening and coalescence processes result in one phase separated cluster in the system after $1.2 \times 10^4\tau$ (inset).

of $\sim 1250\tau$. Beyond this time, Γ has reached a steady state and coarsening and coalescence changes the distribution of aggregate sizes until there is a single phase separated domain by $12000\tau$ (inset).

Although, these growth processes lead to an increase in the maximum aggregate size $N_a^{max}$ (the green dashed curve shows $\frac{N_a^{max}}{N}$ for $\theta = 0.29, \epsilon' = 40$), the fraction of particles in clusters remains relatively constant. The time evolution of $\frac{N_a^{max}}{N}$ (green dashed curve) provides greater insight into this redistribution process. At times greater than $12000\tau$, this ratio becomes equal to Γ meaning that there is one large cluster in the system (inset). Jumps in the green curve are indicative of coalescence events whereas a steady increase points to coarsening.

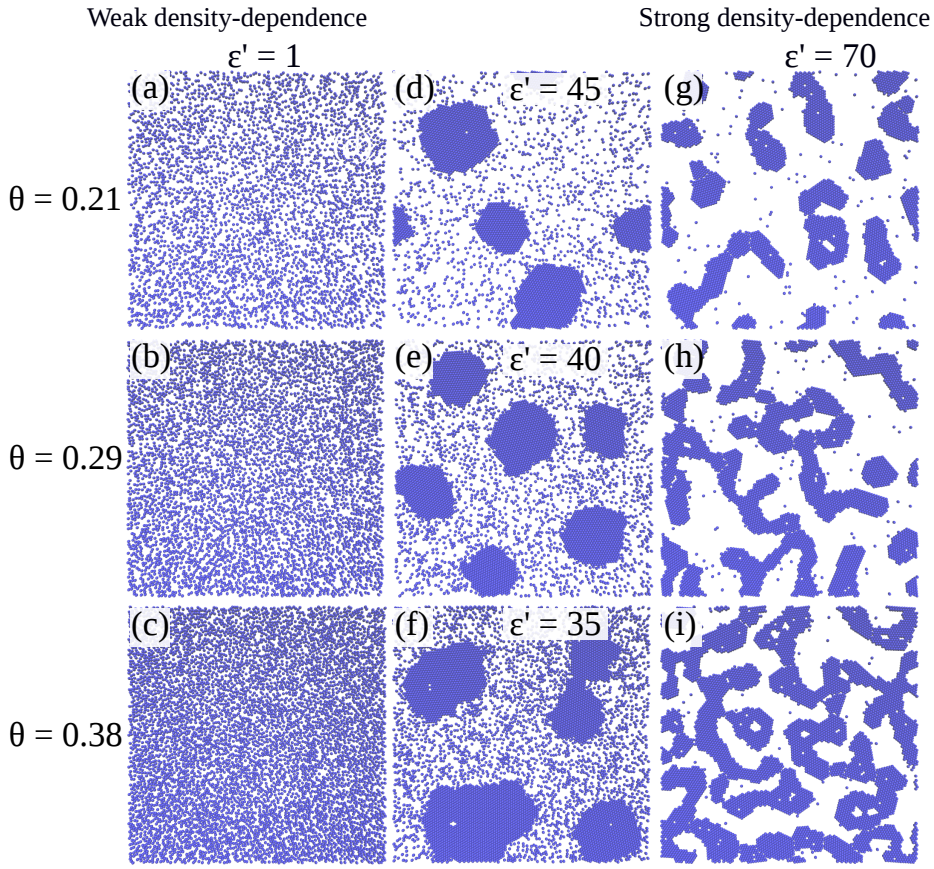


FIG. 5. Simulation snapshots of systems of Brownian particles interacting via density-dependent potential. Snapshots are representative of simulation configurations at times $t_{run} = 2500\tau$ ($\theta = 0.21$) and $t_{run} = 1250\tau$ ($\theta = 0.29$ and $\theta = 0.38$).

### F. Phase separation behaviour and structure emerging from density-dependent simulations

Figure 5 shows configurations at $t_{run}$ for the three area fractions $\theta = 0.21$ ($t_{run} = 2500\tau$), $\theta = 0.29$ ($t_{run} = 1250\tau$), and $\theta = 0.38$ ($t_{run} = 1250\tau$) for values of $\epsilon'$ corresponding to: the "gas-phase" regime ($\epsilon' = 1$); the "phase-separation" regime ($\epsilon' = 45, 40, 35$); and the "gel-like" regime ($\epsilon' = 70$). At $\epsilon' = 1$, the three systems are in a "gas-like" phase with ordering, characterised by the structure factor $S(q)$, consistent with that of a simple colloidal dispersion or hard sphere fluid (Figs. 6 (a)-(c)). At $\epsilon' = 70$, the aggregates are more elongated and tend to "gel-like" states with increasing $\theta$. Well-defined structure in these condensed phases is reflected by the peaks in $S(q)$ (Figs. 6 (g)-(i)).

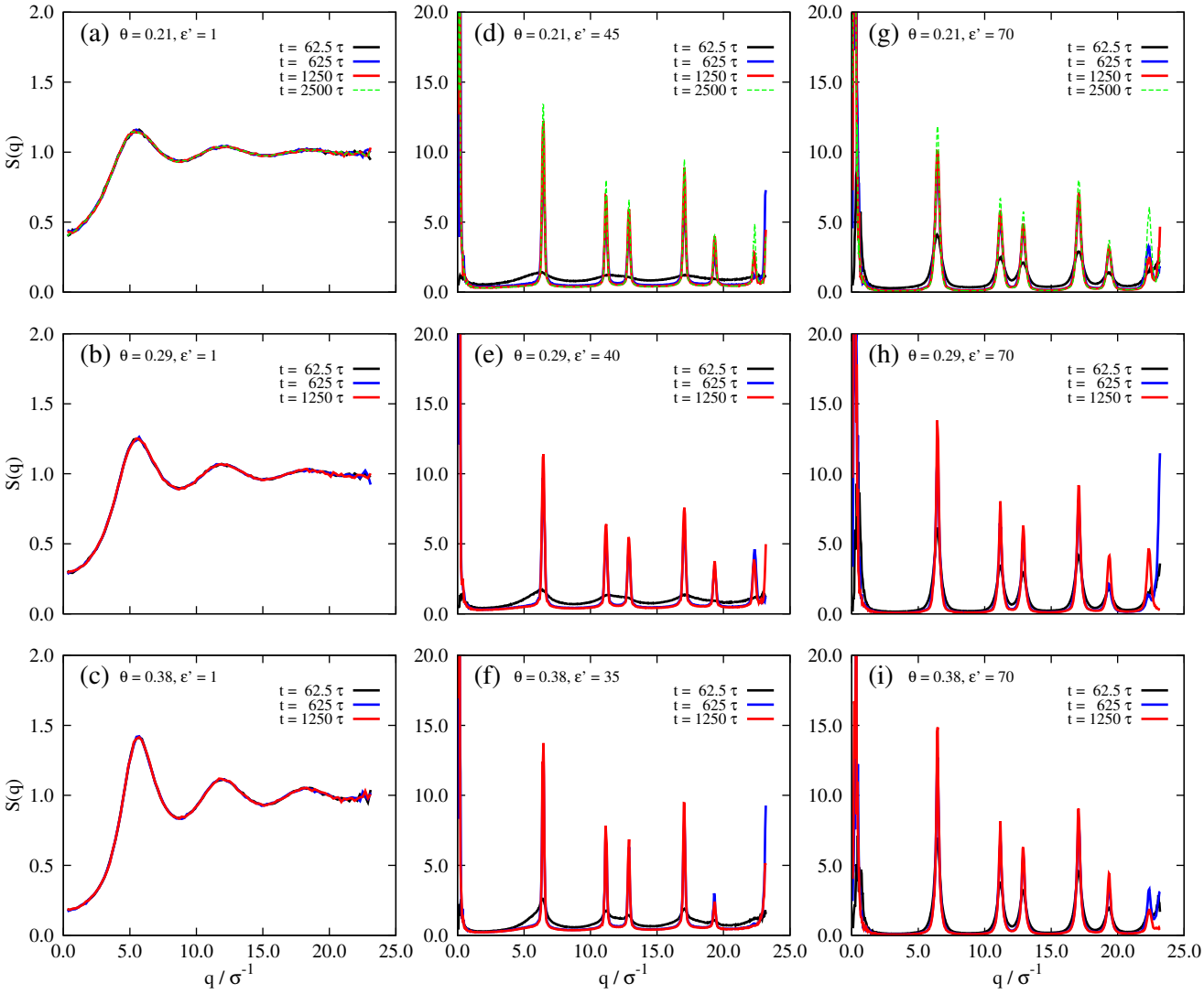


FIG. 6. Static structure factors, $S(q)$, corresponding to various time points during the evolution of the density-dependent simulation towards the states depicted in Fig. 5

.

At intermediate values of $\epsilon'$ (Figs. 5 (d)-(f)), it is clear that the systems are undergoing phase separation into condensed and non-condensed phases, with the emergence of the former being determined by the presence of well-defined peaks in $S(q)$ (Figs. 6 (d)-(f)). Strikingly, the particles are distributed such that condensed phase aggregates are immersed in a dilute "gas".

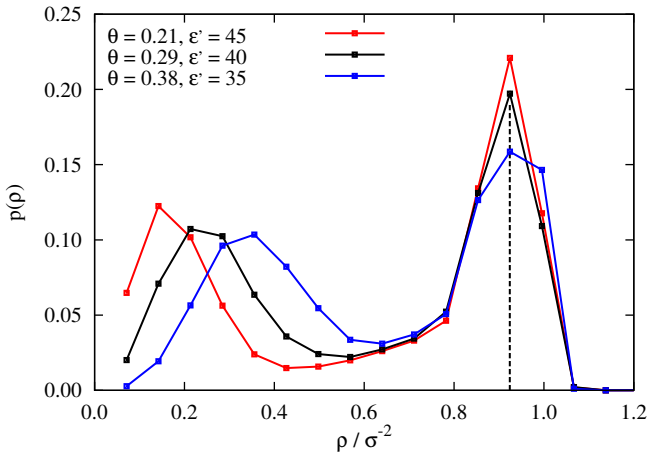


FIG. 7. Normalised probability distributions of the local densities sampled in the 10 final configurations at $2500\tau$ ($\theta = 0.21$) and $1250\tau$ ($\theta = 0.29, 0.38$). The dashed vertical line corresponding to $\rho = 0.924$, gives rise to $\epsilon = 41.58, 36.96, 32.34$ for $\theta = 0.21, 0.29, 0.38$ with which to run density-independent simulations.

### G. Density independent simulations

In any given density-dependent simulation, a range of $\epsilon$ values is sampled by the interacting particles. Therefore, to compare our results to those for systems of particles interacting independently of the density, we carried out density-independent simulations with Lennard-Jones interaction strength $\epsilon$ corresponding to the values of $\epsilon$ sampled (via $\epsilon = \rho(\mathbf{x})\epsilon'$) in the final configurations of the phase separating regimes of our density-dependent simulations (Figs. 5(d)-(f)).

Focusing here on the system with $\theta = 0.29$ and $\epsilon' = 40$, the procedure was performed as follows. From the 10 final configurations at $t_{run} = 1250\tau$ (one of which is shown in Fig. 5 (e)), a normalised distribution, $p(\rho)$, of the local density experienced by each particle (Fig. 7) was constructed. For the 15 values of $\rho$ sampled in these final configurations, a value of $\epsilon$ was generated for each via $\epsilon = \rho(\mathbf{x})\epsilon'$ (see Table I). For each value of $\epsilon$, 10 density-independent simulations were performed. This procedure was repeated for density-independent simulations corresponding to the $\theta = 0.21$, $\epsilon' = 45$, and the $\theta = 0.38$, $\epsilon' = 35$ systems. As will be discussed in more detail below, the value of $p(\rho)$ at each value of $\rho$ was also used as the weight for the construction of a weighted linear superposition of density-independent aggregate size distributions (see Fig. 11(c) of main manuscript).

Figure 7 shows $p(\rho)$ from the density-dependent systems taken at time $t_{run}$. The two peaks in $p(\rho)$ correspond to the phase-separated states shown in Figs. 5(d)-(f). Although increasing $\theta$ has little effect on the location of the high density peak due to limitations in packing, it does have the effect of increasing the density of the "non-condensed" phase. Increasing $\theta$ also leads to a decrease in the bimodal nature of the distributions because more particles are available to sample intermediate values of $\rho$.

| | $\theta = 0.21$ | | $\theta = 0.29$ | | $\theta = 0.38$ | |
|---|---|---|---|---|---|---|
| $\rho$ | $\epsilon = \epsilon' \times \rho$ | $w$ | $\epsilon = \epsilon' \times \rho$ | $w$ | $\epsilon = \epsilon' \times \rho$ | $w$ |
| 0.071 | 3.2 | 0.065 | 2.84 | 0.020 | 2.49 | 0.003 |
| 0.142 | 6.40 | 0.123 | 5.68 | 0.071 | 4.97 | 0.019 |
| 0.213 | 9.59 | 0.102 | 8.52 | 0.107 | 7.46 | 0.056 |
| 0.284 | 12.78 | 0.056 | 11.36 | 0.102 | 9.94 | 0.096 |
| 0.356 | 16.02 | 0.024 | 14.24 | 0.064 | 12.46 | 0.104 |
| 0.427 | 19.22 | 0.015 | 17.08 | 0.036 | 14.95 | 0.082 |
| 0.498 | 22.41 | 0.016 | 19.92 | 0.024 | 17.43 | 0.055 |
| 0.569 | 25.61 | 0.020 | 22.76 | 0.021 | 19.92 | 0.034 |
| 0.640 | 28.8 | 0.026 | 25.60 | 0.027 | 22.40 | 0.031 |
| 0.711 | 32.00 | 0.033 | 28.44 | 0.034 | 24.89 | 0.037 |
| 0.782 | 35.19 | 0.046 | 31.28 | 0.052 | 27.37 | 0.051 |
| 0.853 | 38.39 | 0.134 | 34.12 | 0.131 | 29.86 | 0.126 |
| 0.924 | 41.58 | 0.221 | 36.96 | 0.197 | 32.34 | 0.159 |
| 0.996 | 44.82 | 0.118 | 39.84 | 0.109 | 34.86 | 0.146 |
| 1.067 | 48.02 | 0.002 | 42.68 | 0.002 | 37.34 | 0.001 |

TABLE I. Parameters derived from density-dependent simulations to be used for input (analysis) to (of) density-independent simulations.

Figure 8 shows the aggregate size distributions resulting from density-independent simulations at $t_{run} = 1250\tau$ ($\theta = 0.29, 0.38$) and $2500\tau$ ($\theta = 0.21$). The solid lines represent phase separated regimes in which condensed phase aggregates or gel-like networks are clearly present. The distributions shown with dashed lines, the "non-aggregating regime", fall into

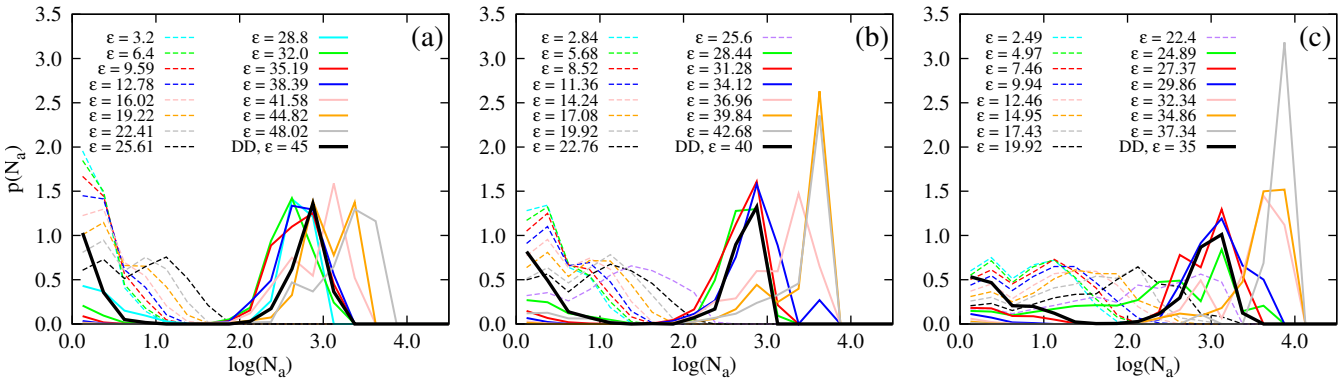


FIG. 8. Distribution of aggregate sizes from density-independent simulations at $2500\tau$ for $\theta = 0.21$ (a) and $1250\tau$ for $\theta = 0.29$ (b) and $\theta = 0.38$ (c). Dashed curves correspond to "non-aggregating" regimes discussed in the text. Each distribution was generated from the final configurations of 10 replicate simulations. The aggregate peak of the purple dashed curve at $\sim \log(3.0)$ in (c) is a result of aggregates present in 4 of the 10 simulations at $\epsilon = 22.4$. Aggregation in this case resulted from nucleation events thus only occurring in a few of the simulations.

three categories: 1) No permanent condensed phase, peaks located at $\log(A) < 1$; 2) Transient aggregates, peaks located between $1 < \log(A) <\sim 2.5$: here the "seeds" of aggregates dissolve upon formation and therefore fail to initialise; and 3) Condensed phase aggregates present in some but not all of the simulations, e.g., at $\theta = 0.29$, $\epsilon = 22.4$ (dashed purple curve in (c)), the peak at $\sim \log(3.0)$ is a result of aggregates that have formed via nucleation in 4/10 simulations. At all three area fractions, the size of the "aggregates" increases with increasing $\epsilon$. It is also evident that the lowest value of $\epsilon$ needed to induce phase separation decreases with increased area fraction $\theta$. In the "non-aggregating" regimes, the increased sampling of transient aggregate sizes with increasing $\theta$ gives rise to flatter distributions. It is evident that the density-independent simulations fail to produce the distributions that emerge from the density-dependent simulations (solid black curves), i.e., two peaks corresponding to condensed and non-condensed phases with little sampling of intermediate aggregate sizes.

Figure 9 shows a representative sample of final configurations resulting from density-independent simulations in the: "non-aggregating" (first column), "aggregating" (middle column), and "gel-like" (third column) regimes. Configurations in the aggregating regimes (middle column) are representative of those distributions in Fig. 8 that most closely resemble

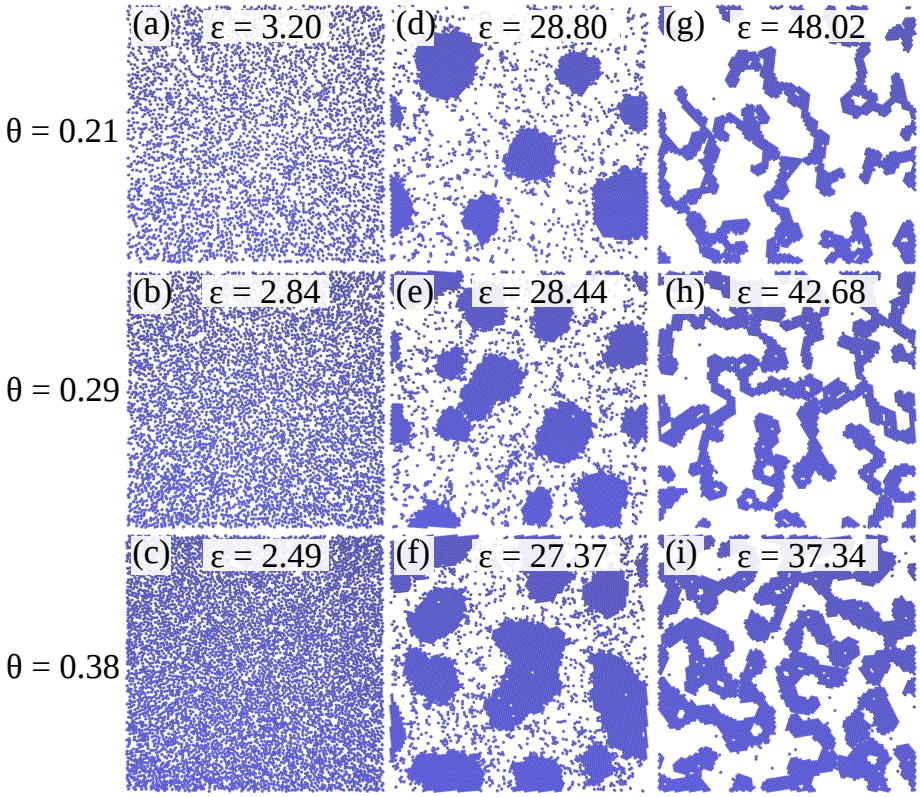


FIG. 9. Simulation snapshots of systems of Brownian particles interacting via standard cut and shifted Lennard-Jones potential. Snapshots are representative of simulation configurations at times $t_{run} = 2500\tau$ ($\theta = 0.21$) and $t_{run} = 1250\tau$ ($\theta = 0.29, 0.38$) for "non-aggregating" (first column), "phase separating" (middle column), and "gel-like" regimes.

the distributions generated from the corresponding density-dependent simulations (solid black curves in Figs. 8). Comparing configurations from the density-dependent and density-independent simulations, (Figs. 5(d)-(f) and Figs. 9(d)-(f)), we see that density-dependent cohesion provides a means by which condensed phase aggregates can coexist with greater numbers of "single particles", i.e., a richer non-condensed phase, evident by the higher value of the "single particle" peak of the black solid curves in Fig. 8.

To assess whether the bimodal distributions generated in our density-dependent simulations $\theta = 0.21, \epsilon' = 45$; $\theta = 0.29, \epsilon' = 40$; and $\theta = 0.38, \epsilon' = 35$ can be viewed as just a simple combination all of the individual distributions in each of Figs. 8(a)-(c), we constructed

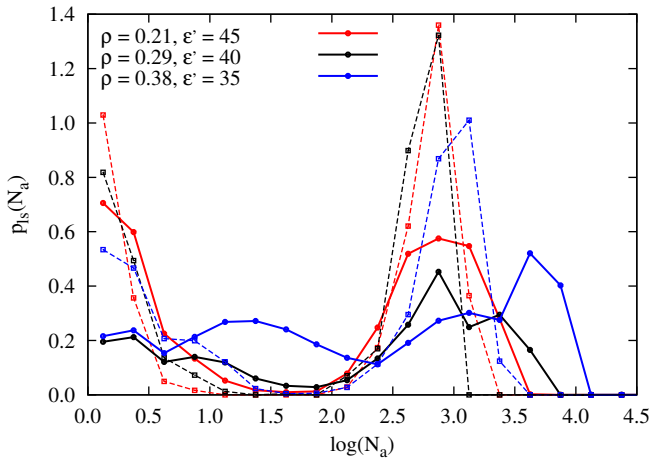


FIG. 10. Aggregate size distributions generated from weighted linear superposition of density-independent simulations (solid curves) corresponding to the phase separating regimes of the density-dependent systems ($\theta = 0.21, \epsilon' = 45$, $\theta = 0.29, \epsilon' = 40$, $\theta = 0.38, \epsilon' = 35$). The original density-dependent aggregate size distributions are shown as dashed curves of the same colour.

weighted linear superpositions of these distributions, $p_{ls}$ (Fig. 10), via

$$p_{ls}(N_a) = \sum_{i=1}^{15} p_{\epsilon_i}(N_a) \times w_{\epsilon_i}, \tag{14}$$

where $p_{\epsilon_i}$ is the aggregate size distribution for a given value of $\epsilon$, and $w_{\epsilon_i}$ is the corresponding weight of that value (Table I) given by the probabilities in Fig. 7, e.g., for the system with $\theta = 0.29$ and $\epsilon' = 40$, the linear superposition distribution at $N_a$ is given by

$$p_{ls}(N_a) = p_{\epsilon_1=3.2}(N_a) \times 0.065 + ... + p_{\epsilon_{15}=42.68}(N_a) \times 0.002. \tag{15}$$

Comparing the resulting linear superpositions with the distributions from the corresponding density-dependent simulations (Fig. 10, solid and dashed curves respectively), it is clear that the aggregation behaviour emerging as a result of density-dependent cohesion is not a simple combination of the various $\epsilon$ values explored. Compared to the density-dependent simulation results, these superpositions show: a much broader range of aggregate sizes; a much more uniform sampling of aggregate sizes; and a greater sampling of larger aggregates.

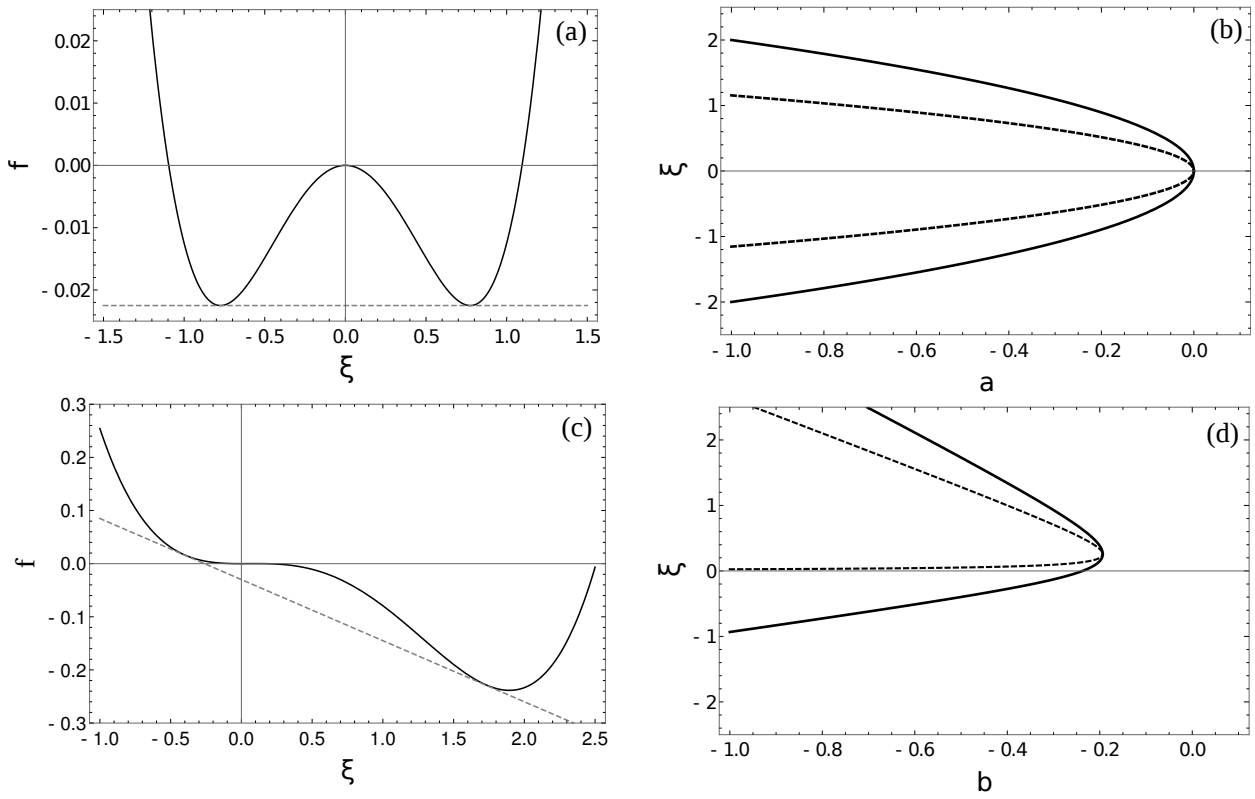


FIG. 11. Thermodynamics of the density-independent and density-dependent Landau systems. (a) Free energy density, $f(\xi)$, for the density-independent system at $a = -1.0$. (b) Full phase diagram of the density-independent system showing binodal (solid black) and spinodal (dashed black) lines resulting from the solution of Eqs. (17) and Eq. (20). (c) Free energy density, $f(\xi)$, for the density-independent system at $b = -0.5$. (d) Full phase diagram of the density-dependent system showing binodal (solid black) and spinodal (dashed black) lines resulting from the solution of Eqs. (17) and Eq. (20). All variables and parameters are in simulation units. Dashed grey lines in (a) and (c) highlight the common tangent construction between the condensed and non-condensed phases, $\xi_2$ and $\xi_1$.

## II. CONTINUUM MODEL

### A. Landau Free Energies and Continuum Model

To ascertain the parameters with which to perform our continuum simulations, we constructed phase diagrams by generating the binodal and spinodal lines in the plane of the critical parameters $a$ for the density-dependent case (and $b$ for density-dependence), and

the global density $\xi_0$. For both density-dependent and -independent systems, the binodal and spinodal lines were generated via examination of the homogeneous part of the Landau free-energy density.

The homogeneous part of the free energy density for the density-independent system is

$$f(\xi) = \frac{a}{2}\xi^2 + \frac{c}{4}\xi^4. \tag{16}$$

where the order parameter, $\xi$, is a measure of the local density. The critical parameter, $a = \psi - \upsilon$ can be positive or negative depending on the interplay between entropic ($\psi$) and attractive ($\upsilon$) parts of the interaction, and governs the transition from disordered to ordered states. The parameter $c$ is a positive constant (0.25) that ensures that the quartic term is the lowest order term required to stabilise the free energy.

In our system, the overall density $\xi_0$ is conserved according to $\int \xi \mathrm{d}\mathbf{x} = \xi_0 A$, where $A$ is total area. Therefore, the system cannot simply adjust its value of $\xi$ in order to minimise the free energy. However, for values of $\xi_0$ that correspond to regions of negative curvature in the free energy, the system *can* lower its free energy by phase separating into coexisting condensed and non-condensed phases with local densities of $\xi_2$ and $\xi_1$ respectively, the values of which satisfy the common tangent construction (grey dashed line Fig. 11(a)).

Mathematically, the common tangent is constructed by equating both the chemical potential, $\mu$, and the pressure, $P$, of the two phases

$$\begin{aligned} \mu_{\xi_1} &= \mu_{\xi_2}, \\ P_{\xi_1} &= P_{\xi_2}, \end{aligned} \tag{17}$$

where

$$\mu(\xi) = \frac{\mathrm{d}f(\xi)}{\mathrm{d}\xi}, \tag{18}$$

and

$$-P = f(\xi) - \mu(\xi)\xi. \tag{19}$$

The solutions of Eqs. (17) for all $\xi$ give rise to a locus of points that form the binodal line (black solid line in Fig. 11(b)). The spinodal line (dashed black line in Fig. 11(b)) was constructed by finding the locus of inflection points of the free energy density by solving

$$\frac{\mathrm{d}^2 f(\xi)}{\mathrm{d}\xi^2} = 0. \tag{20}$$

We follow a similar protocol for constructing the phase diagram for the density-dependent system. The homogeneous part of the Landau free energy density for this system is given by (see main manuscript)

$$f = \frac{\psi}{2}\xi^2 + \frac{b}{3}\xi^3 + \frac{c}{4}\xi^4, \tag{21}$$

where $\psi = 0.05$, and $b \equiv \frac{3}{2}v'$ is the critical parameter that governs the phase transition. The presence of the cubic term makes the free energy potential (Fig. 11(c)) asymmetric when compared to the density-independent case (Fig. 11(a)). The phase diagram for the density-dependent system in Fig. 11(d) was generated by solving Eqs. (17) (via the common tangent construction, grey dashed line Fig. 11(c)) for the binodal line, and solving Eq. 20 for the spinodal line.

In our density-dependent and density-independent continuum models, the common tangent constructions yields non-condensed phases, $\xi_1$, that can become negative when the parameters $a$ and $b$ decrease. To be physically realistic, however, $\xi$, being a measure of the local density, must satisfy the condition that $\xi \geq 0$, and so our continuum model phase diagrams and free energy profiles are truncated at $\xi = 0$ (see main manuscript). In the numerical simulations, this condition is satisfied by setting the chemical potential, $\mu$, equal to $10\xi$ whenever $\xi$ becomes less than zero. This effectively shifts the free energy minimum for the non condensed phase to $\xi_1 = 0.0$.

In our simulations, the dynamics of $\xi$ were modelled using the Cahn-Hilliard equation [4]

$$\frac{\partial \xi(\mathbf{x},t)}{\partial t} = M\nabla^2\left(\frac{\delta}{\delta\xi(\mathbf{x})}\int_A f(\xi(\mathbf{x}))\mathrm{d}\mathbf{x}\right) + \nabla\cdot\mathbf{J}_r, \tag{22}$$

where $M$ is the mobility, the term in brackets is the chemical potential, and $\mathbf{J}_r$ is a random flux which is spatially and temporally uncorrelated, with mean $\langle \mathbf{J}_r(\mathbf{x},t)\rangle = 0$, and variance $\langle \mathbf{J}_{r;\alpha}(\mathbf{x},t)\cdot\mathbf{J}_{r;\beta}(\mathbf{x},t')\rangle = \Lambda\xi\delta_{\alpha,\beta}\delta(\mathbf{x}-\mathbf{x}')\delta(t-t')$, with $\alpha,\beta = x,y$. For simplicity, both $M = 0.01$ and the random noise strength $\Lambda = 0.1$ are kept constant.

Equation 22 was solved on a $256 \times 256$ grid using standard finite difference simulations, with periodic boundary conditions. These simulations were performed using in-house software written in C++. Due to the random flux term in Equation 22, these simulations are stochastic, and therefore, when necessary (see figure captions), many simulation runs were performed in order to generate acceptable statistical data. Stochasticity in each individual simulation was implemented by the use of a random-number generator, each of which was initialised with a different seed.

To map our continuum simulation units to real units we arbitrarily assign length-scales and time-scales to our simulation units such that we can compute an effective diffusion coefficient, $D_{eff}$, with which to compare to the passive (non-motile) diffusion coefficient, $D_p = 0.2\mu m^2 s^{-1}$, of the bacterium *E. coli* [5]. This species of bacteria has a length of $\sim 2\mu m$ and divides approximately every 20 minutes depending on the growth conditions [6].

We used a grid spacing, $l$, of 0.25 simulation length units (SLU), which we can assigned to be equal to $0.5\mu m$, thus giving a characteristic length scale, $l_c$, of $2\mu m$. Much of our analysis was performed after $5 \times 10^6$ simulation steps using a time-step, $\Delta t$, of 0.05 simulation time units (STU) to give run-times, $t_{run}$, of $2.5 \times 10^5$ STU. We assigned this time to be equal to 20 minutes ($1.2 \times 10^3 s$) in order to work within experimental time-scales, in which the number of cells is conserved (no growth and division). This gives rise to a characteristic time-scale, $t_c$, of $\frac{1.2\times10^3}{2.5\times10^5} = 4.8 \times 10^{-3}$ seconds. We can use these characteristic time- and length- scales to compute the effective diffusion coefficient via $D_{eff} = \frac{l_c^2}{t_c} D_s$, where $D_s = Ma$ (simulation units of energy times inverse time). Using $M = 0.01$ and $a = \psi = 0.05$ (for the density-dependent Landau free energy density), the value of $D_{eff}$ for our continuum simulations is $0.42\mu\mathrm{m}^2\mathrm{s}^{-1}$ which is comparable to that of *E. Coli*.

### B. Aggregate growth in the continuum Model

To compute aggregate sizes and aggregate size distributions in the continuum model for the density-independent ($a = -1.0$) and density-dependent ($b = -.05$) systems, the spatial continuum of densities was converted to a binary representation by considering only those pixels that have a density value of $\xi > 0.4$. The size of the aggregates, $A$, was then computed by analysing the connectivity between these selected pixels (or points with $(x, y)$ coordinates), via the same linked-list method [7] used for analysing the particle-based simulations.

Figure 12(a) shows the amplification factor (see main manuscript) for the density-dependent (red curve) and density-independent (blue curve) homogeneous Landau free energy densities at $\xi = 0.3$. The maximum of this function, which sets length-scale of the structures formed during spinodal decomposition, occurs at larger value of $q$ ($\sim 1.6$) in the density-independent system than in the density-dependent system ($q \sim 0.7$). Due to the reciprocal space dependence ($q$) of the amplification factor, this suggests that the

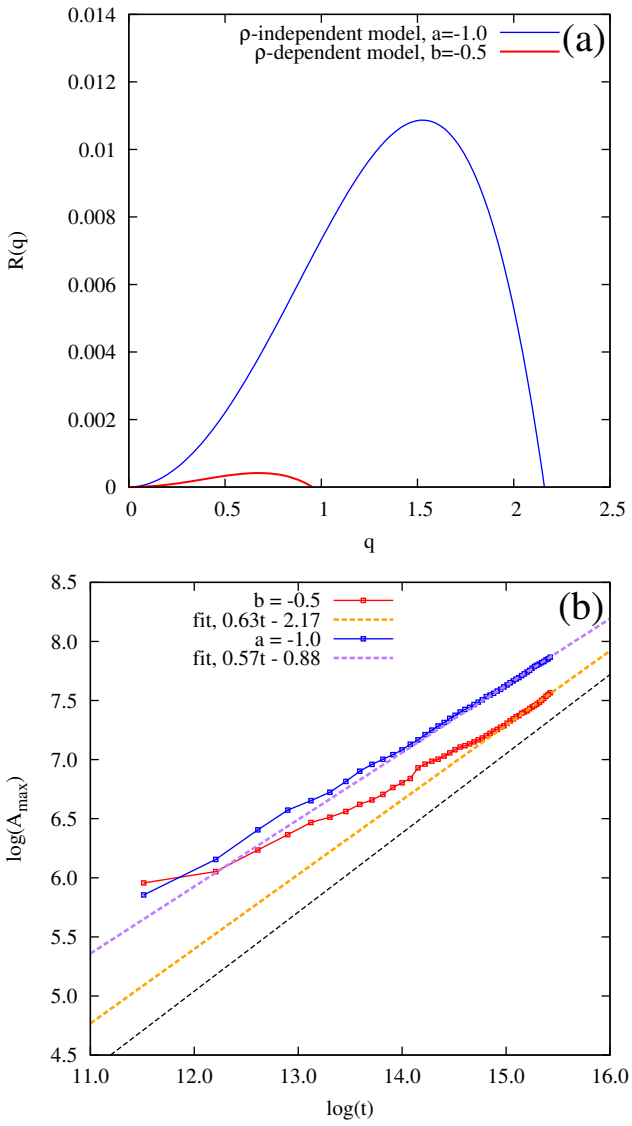


FIG. 12. Aggregate growth. (a) Amplification factor, $R(q)$, for the density-dependent (red curve) and density-independent (blue curve) homogeneous Landau models. (b) Growth of the maximum aggregate size ($A_{max}$) as a function of time in the numerical simulations. The growth curves generated were averaged over several repeated simulations, 4 in the density-independent system, and 5 in the density-dependent system. All units are in simulation units (SU).

structures formed in the very early stages of phase separation should be narrower in the density-independent system compared to density-dependent system; this is evident from Fig. 9 of the main manuscript. Figure 12(b) shows how the growth of the maximum cluster size in both the density-dependent (red curve) and density-independent systems (blue

curve) scale with time. In classic models of phase separation in diffusive systems without hydrodynamic interactions, one would expect the typical domain length, computed from the structure factor, to scale as $t^{1/3}$, and thus area or number of particles $N$ to scale as $t^{2/3}$. Although, here, we have assessed cluster growth, with respect to the maximum cluster size in the system $A_{max}$, the scaling in Fig.12(b) is commensurate with such models.

### C. Density and aggregate size distributions for switched simulations

The time evolution of the density distributions corresponding to the simulation snapshots in Fig. 9 of main manuscript are shown in Fig. 13. The similarity in the distributions between (c) and (l), and, (f) and (i), strengthens the notion, pointed out in the main manuscript, that trajectory history has little influence on the long term dynamics of phase separation in the density-dependent system, and that it is the governing thermodynamics that determine the behaviour. This if further supported by the fact the initial state has little effect on the aggregate size distributions (Fig. 14).

### D. Restoration of fluctuation dissipation theorem

In Eq. (12) of the main manuscript, it was noted that the choice of the prefactor, $\Lambda\xi(\mathbf{x})$ in the spatially and temporally uncorrelated random flux

$$\begin{aligned} \langle \mathbf{J}_r(\mathbf{x},t)\rangle &= 0 \\ \langle \mathbf{J}_{r;\alpha}(\mathbf{x},t)\cdot\mathbf{J}_{r;\beta}(\mathbf{x},t')\rangle &= \Lambda\xi\delta_{\alpha,\beta}\delta(\mathbf{x}-\mathbf{x}')\delta(t-t') \end{aligned} \tag{23}$$

violated the fluctuation-dissipation theorem (FDT) linking noise strength and mobility via

$$\langle \mathbf{J}_{r;\alpha}(\mathbf{x},t)\cdot\mathbf{J}_{r;\beta}(\mathbf{x},t')\rangle = 2_B T m\delta_{\alpha,\beta}\delta(\mathbf{x}-\mathbf{x}')\delta(t-t'). \tag{24}$$

This violation is acceptable in our study given that the dynamics of polymer secretion outlined from Eqs. (1) to (5), will typically put the system out of equilibrium. That said, however, we also did a quick qualitative comparison between the density-dependent and independent systems ($b=-0.5, a=-1.0$) at an overall system density $\xi_o$ with FDT restored (Eq. 23). We found that the condensed phase regions formed more rapidly in the density-independent system from elongated structures typically associated with those

formed in the early stages of spinodal decomposition (Figs. 15(a) to (c)). These structures rapidly contract to small aggregates that then coarsen and coalesce with time. In the density-dependent system however, the formation of these elongated structures is not evident, rather phase separation proceeds via the formation of larger more rounded aggregates (Figs. 15(d) to (f)).This behaviour is qualitatively similar to that outlined in the main manuscript in which the FDT was violated.

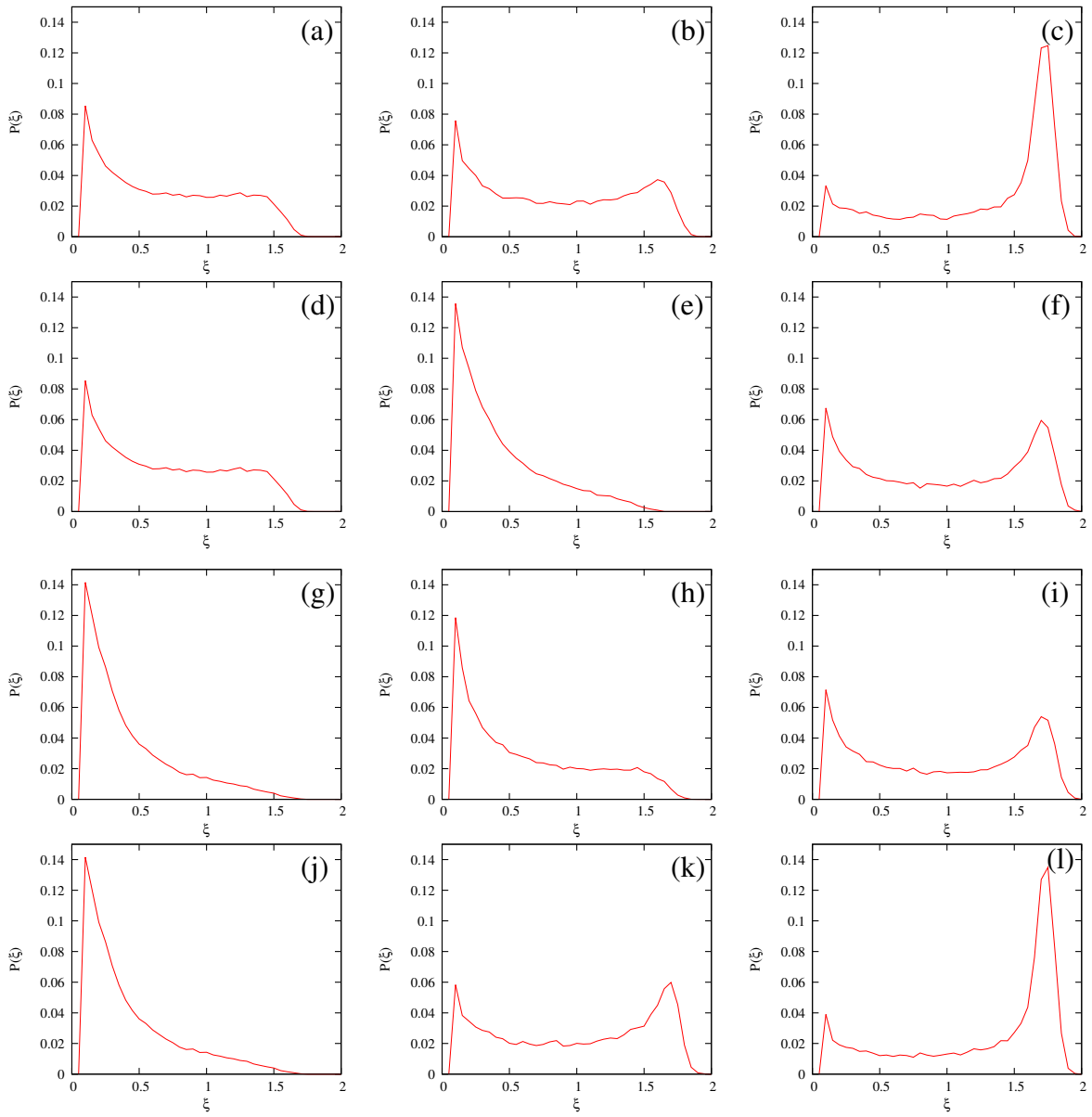


FIG. 13. Time evolution of the probability distribution, $P(\xi)$, corresponding to Fig. 9 of the main manuscript for the "non-switched" (1st and 3rd row) vs "switched simulations" (2nd and 4th row). 1st row (top)- Density-independent simulation initialised with a configuration from a density-independent simulation at time $t = t_{ps} = 550$ SU. 2nd row- Density-dependent simulation initialised with a configuration from a density-independent simulation at time $t = t_{ps} = 550$ SU. 3rd row- Density-dependent simulation initialised with a configuration from a density-dependent simulation at time $t = t_{ps} = 3500$ SU. 4th row (bottom)- Density-independent simulation initialised with a configuration from a density-dependent simulation at time $t = t_{ps} = 3500$ SU. Columns (a, d, g, j), (b, e, h, k), and (c, f, i, l) correspond to times $t = 0$ SU, $t = 1500$ SU, and $t = 50000$ SU respectively.

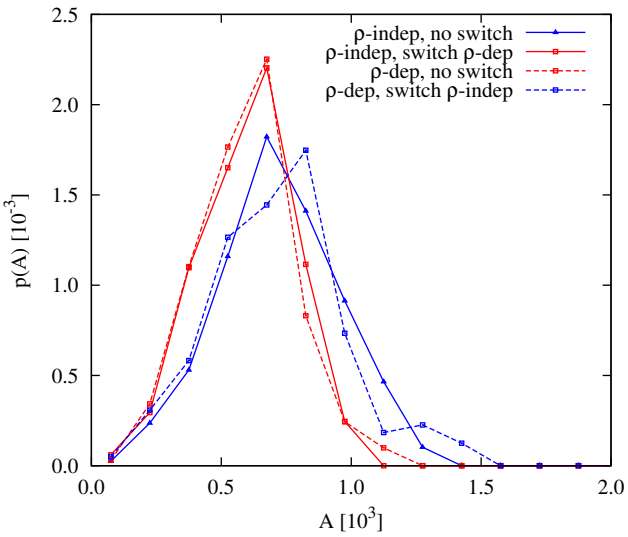


FIG. 14. Distribution of aggregate sizes corresponding to the final configurations ($t = 50000$) of Fig. 10(c), (f), (i), (l) in the main manuscript for the switched and non-switched simulations. Solid blue curve corresponds to (c), solid red curve corresponds to (f), dashed blue corresponds to (l), and dashed red corresponds to (i).

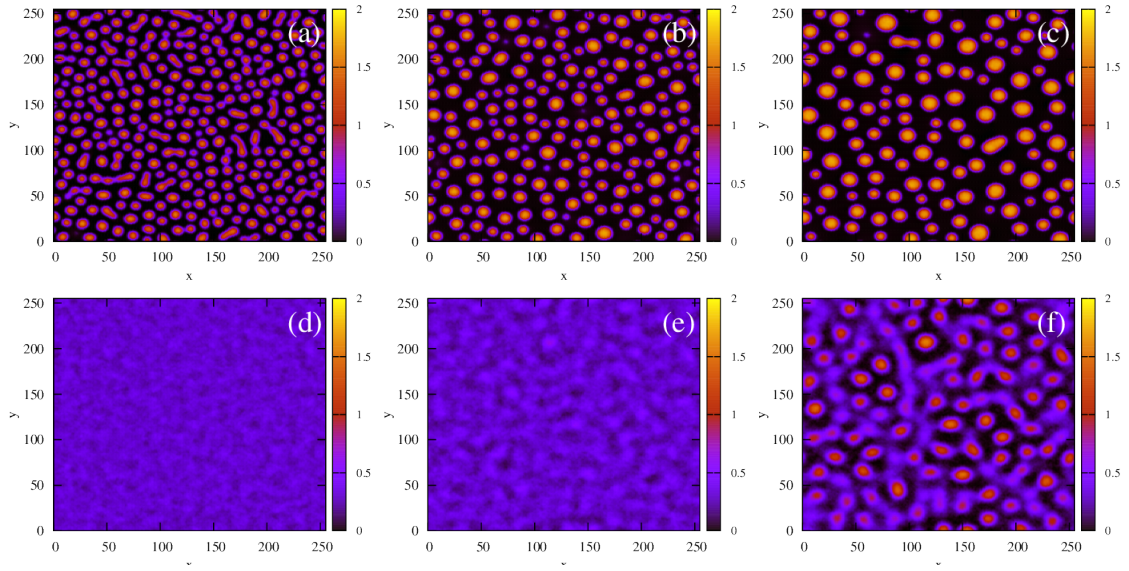


FIG. 15. Simulation snap-shots showing the time evolution of the density-independent (a-c) and -dependent (d-e) systems with fluctuation-dissipation restored. (a) Density-independent, $t = 500$ SU. (b) Density-independent, $t = 1500$ SU. (c) Density-independent, $t = 3500$ SU. (d) Density-dependent, $t = 500$ SU. (e) Density-dependent, $t = 1500$ SU. (f) Density-dependent, $t = 3500$ SU.

[1] M. P. Allen and D. Tildesley, *Computer Simulations of Liquids*, Oxford Univeristy Press, 1997.

[2] P. Grassia, E. Hinch and L. C. Nitsche, *J. Fluid Mech.*, 1995, **282**, 373–403.

[3] J. D. Weeks, D. Chandler and H. C. Andersen, *The Journal of Chemical Physics*, 1971, **54**, 5237–5247.

[4] J. W. Cahn and J. E. Hilliard, *J. Chem. Phys.*, 1958, **28**, 258.

[5] H. Berg, *E. coli in Motion*, Springer New York, 2008.

[6] W. Donachie, K. Begg and L. M. Vicente, *Nature*, 1976, **264**, 328.

[7] S. Stoddard, *J. Comp. Phys.*, 1978, **27**, 291–293.